MATERIALS CHEMISTRY FRONTIERS

CHINESE CHEMICAL SOCIETY

ROYAL SOCIETY OF CHEMISTRY

RESEARCH ARTICLE

View Article Online
View Journal | View Issue

Cite this: *Mater. Chem. Front.*, 2023, **7**, 4952

$FeNi_3$ nanoparticles for electrocatalytic synthesis of urea from carbon dioxide and nitrate†

Tong Hou,[ab] Junyang Ding,*[c] Hao Zhang,[c] Shanshan Chen,[c] Qian Liu,[d] Jun Luo[e] and Xijun Liu*[ab]

Received 1st June 2023,
Accepted 13th August 2023

DOI: 10.1039/d3qm00627a

rsc.li/frontiers-materials

Due to the environmental pollution and high energy consumption associated with the conventional industrial Bosch–Meiser method, electrocatalytic urea synthesis emerges as a promising and sustainable alternative route. In this work, we constructed and utilized nitrogen-doped porous carbon loaded with bimetallic $FeNi_3$ alloy nanoparticles as an efficient electrocatalyst for synthesizing urea from carbon dioxide (CO_2) and nitrate (NO_3^-). The created $FeNi_3$ alloy within FeNi/NC served as the active site for the C–N coupling reaction, generating a higher urea yield of 496.5 μg h^{-1} $mg_{cat.}^{-1}$ with a correlating faradaic efficiency (FE) of 16.58% at −0.9 V *versus* the reversible hydrogen electrode (*vs.* RHE), when in comparison to monometallic Fe/NC and Ni/NC catalysts. Moreover, we also monitored the urea generation process *via in situ* Raman spectroscopy technology, which enabled the identification of two critical reaction species, namely O–C–O and N–C–N, inferring that C–N coupling acted as the key reaction step.

1. Introduction

Urea, an indispensable nitrogen source in agricultural fertilizers, plays a pivotal role in promoting robust crop growth.[1–4] However, the conventional industrial technique employed for urea production necessitates the harsh reaction between ammonia (NH_3) and CO_2 with extreme conditions of elevated temperatures (150–200 °C) and pressures (100–200 atm).[5–7] Regrettably, this approach not only engenders substantial energy consumption but also exacerbates environmental concerns by contributing to the release of CO_2 emissions.[8–10] To surmount these formidable challenges and foster the principles of sustainable development, it is imperative to explore alternative methodologies enabling the synthesis of urea under milder conditions.[10–12] One particularly promising avenue lies in harnessing the potential of electrocatalytic C–N coupling to urea, which effectively utilizes CO_2 and NO_3^- as reactants and operates under ambient conditions. However, the main issues present with NO_3^- pollutants, *i.e.*, low concentration, complicated composition, heavy metals and chemical oxygen demand, will lead to decline in electrocatalytic performance.[13] For other nitrogen sources, the intrinsic chemical inertness and low solubility of N_2 significantly restrict urea yield and faradaic efficiency (FE);[14] NO_2^- is unstable and susceptible to nitrate formation in aqueous solution.[15] Thus, NO_3^- is more appealing from an application standpoint as a nitrogen source for the electrocatalytic production of urea with CO_2. This indicates that the innovative approach of electrocatalytic synthesis of urea, which holds tremendous prospects for attaining efficient conversion to urea while significantly alleviating the demands for energy resources, still has a number of challenges that need to be addressed.[16–19]

As widely acknowledged, the composition and structure of catalysts are of utmost significance in the realm of electrocatalytic urea synthesis.[20–22] Such as, the metal alloying strategy promotes electronic interactions among the various components, which facilitates the creation of more different active sites for the electrocatalytic reaction to cooperatively activate the reactants/intermediates and reduce the occurrence of side reactions.[23–25] Thus, alloy catalysts have been widely applied in electrochemical application.[26–28] As an exemplification of this concept, Wang *et al.* reported an AuPd nanoalloy, with Pd and Au as the active sites for carbon dioxide reduction reactions (CO_2RR) and nitrate reduction reactions (NO_3RR), respectively, to synergistically catalyze the formation of urea by C–N

[a] *MOE Key Laboratory of New Processing Technology for Non-Ferrous Metals and Materials, and Guangxi Key Laboratory of Processing for Non-Ferrous Metals and Featured Materials, School of Resource, Environments and Materials, Nanning 530004, China. E-mail: xjliu@gxu.edu.cn*
[b] *Guangxi Key Laboratory of Electrochemical Energy Materials, School of Chemistry and Chemical Engineering, Guangxi University, 100 Daxue Road, Nanning 530004, China. E-mail: junyangdingde18@163.com*
[c] *Institute for New Energy Materials & Low-Carbon Technologies, School of Materials Science and Engineering, Tianjin University of Technology, Tianjin 300384, China*
[d] *Institute for Advanced Study, Chengdu University, Chengdu 610106, Sichuan, China*
[e] *ShenSi Lab, Shenzhen Institute for Advanced Study, University of Electronic Science and Technology of China, Longhua District, Shenzhen 518110, China*
† Electronic supplementary information (ESI) available. See DOI: https://doi.org/10.1039/d3qm00627a

coupling reaction.[26] Given the great potential of alloy electrocatalysts in the relevant electrocatalytic reaction of urea generation, and through extensive literature it can be found that bimetallic FeNi catalysts are expected to be the superior candidates for urea synthesis, *i.e.* nickel-based catalysts exhibit excellent performance in CO_2RR, whereas iron-based catalysts display remarkable efficacy in NO_3RR. For CO_2RR, Chen *et al.* developed a nickel phthalocyanine (NiPPc) electrocatalyst, achieving up to 99.8% selectivity of CO.[29] Similarly, Lu *et al.* introduced a pyridine nitrogen-coated nickel nanoparticle with core–shell structure, showing up to 90% FE in reducing CO_2 to CO.[30] For NO_3RR, Zhang *et al.* used ultra-thin graphene nanosheets as protective armor, ensuring long-term catalytic performance by preventing oxidation and leakage of iron nanoparticles.[31] Cu-doped hematite particles also achieved nearly 100% FE in converting NO_3^- to NH_3.[32] While cobalt-doping can precise tuning of the d-band center of $Fe@Fe_2O_3$, thus achieving NH_3 selectivity up to 99%.[33]

Taking into consideration the individual advantages of Fe-based and Ni-based catalysts showcased in the aforementioned respective reactions, this study designed a $FeNi_3$ alloy catalyst (FeNi/NC) capable of simultaneously adsorbing and activating CO_2 molecules and NO_3^- ions, leading to efficient urea synthesis through the construction of C–N coupling active sites. The synergistic effect between Fe and Ni components yields remarkable improvements in the electrochemical synthesis of urea, with an impressive urea yield of 496.5 μg h^{-1} $mg_{cat.}^{-1}$ and a corresponding FE of 16.58%. This work emphasizes a feasible methodology for sustainable urea synthesis through metal alloying and C–N coupling.

2. Experimental section

2.1 Chemicals

Polyvinylidene chloride (PVDC), sodium ethylate (C_2H_5ONa, 96%) were bought from MACKLIN; lignin (Alkaline), Melamine (99%), and Nickel chloride hexahydrate ($NiCl_2{\cdot}6H_2O$) were received from Aladdin Biochemical Technology; Iron chloride ($FeCl_3$), nitrate of potash (KNO_3, ≥99.99% metals basis), potassium hydroxide (KOH) were acquired through Sinopharm Chemical Reagent Co., Ltd; Carbon papers (HCP020N) were provided from Hesen company (Shanghai, China) and rinsed with acetone, ethanol, and distilled water before being used. Urease was purchased from Sigma, its activity and batch number are 20KU and Lot#SLCJ5647, respectively. Milli-Q ultrapure water (>18 Ω) was used in all experiments. All chemicals were used without further purification.

2.2 Synthesis of FeNi/NC

Firstly, 1 g PVDC, 1 g lignin, 1 g KOH, 0.5 g melamine, 2.04 g C_2H_5ONa, 0.3 g $FeCl_3$, 0.15 g $NiCl_2{\cdot}6H_2O$ were meticulously mixed in an agate mortar and thoroughly ground. The resulting viscous liquid was then solidified by freezing it with liquid nitrogen and subsequently transferred to a freeze dryer where it underwent an 8 hour drying process. Following that, the carbonation procedure was initiated. The prepared precursors were carefully transferred to a quartz boat and placed in a tube furnace under a N_2 atmosphere. The temperature was gradually increased at a rate of 5 °C per minute until reaching 950 °C, and the samples were maintained at this temperature for 2 h. Subsequently, the excess fractions of Fe and Ni were eliminated by subjecting the black powder to a reaction with 1 M H_2SO_4 at 90 °C for a duration of 12 h. The resulting powder was washed with deionized water until reaching neutrality and subsequently dried under vacuum conditions. Lastly, the obtained powder was once again subjected to carbonization at 950 °C under a N_2 atmosphere for 2 h, resulting in the final formation of the FeNi/NC catalyst. In the aforementioned synthesis process, a combination of C_2H_5ONa and KOH can be employed to eliminate the Cl element from PVDC. Melamine is served as the nitrogen source.[34] It is worth noting that lignin, which contains abundant hydroxyl and carboxyl groups, plays a vital role in effectively adsorbing metal ions and facilitating the dispersion of metal elements on the nitrogen-doped carbon carrier during the carbonization.[35,36]

2.3 Synthesis of Fe/NC

The synthesis procedure for Fe/NC followed a similar process to that of FeNi/NC, with the only difference being the use of 0.389 g of $FeCl_3$ instead of the combination of 0.3 g of $FeCl_3$ and 0.15 g of $NiCl_2{\cdot}6H_2O$.

2.4 Synthesis of Ni/NC

The synthesis procedure for Ni/NC is the same as that for FeNi/NC, except that 0.3 g of $FeCl_3$ and 0.15 g of $NiCl_2{\cdot}6H_2O$ are replaced by 0.570 g of $NiCl_2{\cdot}6H_2O$.

2.5 Materials characterization

The morphology of catalysts was investigated by field emission Scanning electron microscopy (SEM, ZEISS VLTRA-55) and transmission electron microscopy (TEM, FEI Tecnai G2 F20). The Raman spectra were acquired on a Renishaw in *via* Raman microscope with the 532 nm laser. X-ray diffraction (XRD) measurements were performed on a D8 ADVANCE X-ray diffractometer (Bruker). The X-ray photoelectron spectroscopy (XPS) analyses were performed with an ESCALAB 250 Xi X-ray photoelectron spectrometer. The gaseous products for electrocatalytic reaction were quantified on a GC9790 plus (FULI instruments). The ^1H NMR spectra were measured on an Ascend 800 MHz NMR spectrometer (Bruker) equipped with an ultralow temperature probe.

2.6 Electrochemical characterization

All electrochemical characterizations were conducted using a CHI 760E workstation integrated with a three-electrode configuration within a two-compartment cell, which was divided by a Nafion 117 membrane. The catalyst loading on the carbon paper (Hesen, HCP-020) was served as the working electrode, and the carbon rod and the Ag/AgCl (saturated KCl solution) were applied as the counter and reference electrodes, respectively. For the preparation of catalyst ink, 2 mg of catalyst

was dispersed in the mixed solution of deionized water (500 μL), isopropanol (450 μL) and 5 wt% Nafion (50 μL). After ultrasonic treatment for 1 h, the homogenous ink was formed and 50 μL of the catalyst ink was drop-casted onto the carbon paper with a geometric surface of 1 × 1.5 cm^2, thus the catalyst loading is 0.1 mg cm^{-2}.

For the electrocatalytic synthesis of urea, the electrolyte was initially purged with CO_2 (purity: 99.999%, flow rate: 100 sccm) for 0.5 h for degassing and CO_2 saturation. The flow rate was then adjusted to 30 sccm and the continuous feeding of CO_2 was kept during the electrochemical test of 1 h. Then, the cathode electrolyte was extracted for further analyzation. The all applied potentials in this work have been converted to the RHE scale:

$$E(vs.\ \mathrm{RHE}) = E(vs.\ \mathrm{Ag/AgCl}) + 0.0591 \times \mathrm{pH} + 0.197$$

The pH was 3.9 or 6.8 in the presence or absence of CO_2 saturation, respectively.

***In situ* Raman test.** A three-electrode flow cell with a quartz window (C031-3, Gaoss Union, Tianjin) was applied to collect in Raman spectra data (Renishaw: laser, λ = 532 nm; power, 5 mW). A gold plate loaded with powder catalyst, Ag/AgCl (Saturated KCl) and graphite rod were used as working, reference and counter electrode, respectively. The cathode and anode chambers were separated by the membrane (Nafion 117), and a CO_2-saturated 0.1 M KNO_3 electrolyte was continuously passed into the cathode chamber. The Raman signals at different applied potentials or electrolysis time were recorded using a 10 s acquisition time.

2.7 Determination of urea and NH_3

The generated NH_3 was quantified using the indophenol blue method. Three aqueous colorants were employed: (a) 1 M NaOH (5 wt% sodium citrate, 5 wt% salicylic acid); (b) 0.05 M NaClO; (c) 1 wt% sodium nitroferricyanide. Subsequently, the solution was added sequentially with the following volumes: 2 mL electrolyte, 2 mL (a) 1 mL (b) and 0.2 mL (c). The resulting mixture was then incubated under dark environment for 2 h, followed by the absorbance measurement, and obtain the amount of NH_3 according to the calibration curve between NH_3 concentration and the absorbance at 662 nm.[10] The concentration of urea was determined utilizing the urease decomposition.[34,35] The 1.8 mL electrolyte comprising urea underwent hydrolysis employing 0.2 mL urease (5 mg mL^{-1}) for a duration of 1 h at 37 °C. The quantification of NH_3 concentration before and after the hydrolysis experiment was accomplished utilizing the previously established calibration curve of NH_3. The quantification of urea quantity was based on the stoichiometric conversion, whereby 1 urea molecule yields 1 CO_2 and 2 NH_3.

Calculations of urea yield and the faradaic efficiency. The mole concentration of yielded urea (m_{urea}) can be calculated as followed:

$$m_{\mathrm{urea}} = \frac{(m_2 - m_1)60.06}{2 \times 17}$$

m_1 and m_2 are the NH_3 concentrations before and after the urease decomposition experiment, respectively.

The urea yield rate of urea was calculated from the following equation:

$$R(\mathrm{urea}) = \frac{cv}{tm}$$

R (urea) represents the urea yield (mg h^{-1} $mg_{cat.}^{-1}$); c for urea mass concentration (mg mL^{-1}); v for electrolyte volume (mL); t presents the reaction time (h); m for catalyst mass (mg).

The FE of urea can be acquired through the following equation:

$$\mathrm{FE}(\%) = \frac{nFcv}{60.06Q} \times 100$$

where F for the Faraday constant (96485.3 C mol^{-1}), Q for electric quantity, c for generated urea concentration, v for electrolyte volume, n is the number of electron transfer, which is 16 for electro-coupling of CO_2 and NO_3^-.

Calculations of the NH_3 faradaic efficiency. The FE of NH_3 was calculated through the following equation:

$$\mathrm{FE}(\%) = \frac{nFcv}{17Q} \times 100$$

where F denotes the Faraday constant (96 485.3 C mol^{-1}), Q for electric quantity, c for generated NH_3 concentration, v for electrolyte volume, and n represents the number of electron transfer, which is 8.

2.8 Determination of CO and H_2

The thermal conductivity detector (TCD) on the gas chromatograph is used to identify H_2, while its the flame ionization detector (FID) is used to detect CO and other hydrocarbons.

Calculations of the CO and H_2 faradaic efficiency. The FE of gas product is calculated as following equation:

$$\mathrm{FE}(\%) = \frac{nF\frac{S_1 C_2}{S_2}}{I\frac{RT}{PV}} \times 100$$

where n represents the number of transferred electrons (n = 2), v (mL min^{-1}) represents the gas flow rate of CO_2, and the S_1 represents the product peak area, the C_2 represents the standard gas product concentration, the S_2 represents the standard gas product peak area. The i is the total current measured during gas collection. P = 101 325 Pa, F = 96 485 C mol^{-1}, R = 8.314 J mol^{-1} K^{-1}, and T = 298.15 K.

2.9 Determination of NO_2^-

4 g of aminobenzenesulfonamide, 0.2 g of *N*-(1-teayl) ethylenediamine dihydrochloride, 10 mL of phosphoric acid (ρ = 1.685 g mL^{-1}), and 50 mL of deionized water were mixed well as a coloring agent. Take 0.2 mL of electrolyte, dilute it to 5 mL, then add 0.1 mL of colouring agent and mix thoroughly. After the reaction at room temperature for 20 min, the absorption spectrum was measured by UV-Vis spectrophotometer, and recorded the absorption intensity at 540 nm. The NO_2^-

standard concentration-absorbance curves were obtained using a series of standard solutions of different concentrations of KNO_2.[37]

Calculations of NO_2^- faradaic efficiency. The FE of NO_2^- is calculated as the following equation:

$$\mathrm{FE}(\%) = \frac{nFcv}{46Q} \times 100$$

where F stands for the Faraday constant (96 485.3 C mol^{-1}), Q for electric quantity, c for produced NO_2^-, v is electrolyte volume, n for the number of electron transfer, which is 2.

3. Results and discussion

The fabrication process of FeNi/NC was illustrated in Fig. 1a. After the metal source, carbon source, and nitrogen source were thoroughly mixed, this mixture was sequentially subjected to the procedures of freeze-drying, carbonization, acid washing, and pyrolysis to obtain the FeNi/NC sample. And the detailed procedures could be acquired in the Experimental section. The morphology of the FeNi/NC, Fe/NC and Ni/NC catalysts were characterized by SEM in Fig. 1b and Fig. S1 (ESI†), which revealed a porous structure with thinner carbon nanosheets randomly anchored or wrapped with metallic nanoparticles (from ~20 nm to 200 nm in diameter). And high-angle annular dark-field scanning TEM (HAADF-STEM) also clearly showed uniform dispersion of the brighter metal nanoparticles in the porous carbon matrix (Fig. 1c). Meanwhile, in Fig. 1e–i, elemental mapping showed that C, N, and O elements are well distributed overall, while Fe and Ni elements are more concentrated on the alloy nanoparticles. Moreover, the interplanar spacing of 0.355 nm and 0.335 nm, corresponding to the (100) plane of $FeNi_3$, and (111) plane of graphite carbon, respectively, can be seen by high-resolution TEM (HRTEM) in Fig. 1d and Fig. S2 (ESI†). Therefore, it can be inferred that FeNi/NC forms a nitrogen-doped porous carbon structure with a large specific surface area of randomly distributed $FeNi_3$ alloy nanoparticles, which facilitates the exposure of active sites and promotes electron transfer and mass transfer.[38]

XRD analysis was employed to investigate the composition properties of the theses materials. As shown in Fig. 2a, the diffraction peaks of $FeNi_3$ (PDF#88-1715), Fe_3O_4 (PDF#75-0449), and graphitic carbon (PDF#75-2078) were observed in the XRD spectra of FeNi/NC, indicating the successful generation of a $FeNi_3$ alloy. However, for Fe/NC and Ni/NC (Fig. S3 and S4, ESI†), only the respective Fe (PDF#87-0721), Fe_3O_4 (PDF#75-0033) and Ni (PDF#87-0712) metals were found. Fig. 2b showed the Raman spectra of these samples to characterize their degree of graphitization, which exists two typical D (~1350 cm^{-1}) and G (~1580 cm^{-1}) bands associated with lattice carbon defects and sp^2 hybridized carbon, respectively. Among them, Fe/NC (1.01), Ni/NC (1.02), and FeNi/NC (1.06) exhibited similar intensity ratio of I_D/I_G, indicating that there is no significant difference in the degree of graphitization of these samples.[39] Fig. 2c presented the Fe 2p XPS spectrum, where four peaks at 733.5, 728.3, 725.7, and 723.9 eV correspond to Fe^{3+} (satellite), Fe^{2+} (satellite), Fe^{3+}, and Fe^{2+} in the Fe $2p_{1/2}$ region, respectively. And in the Fe $2P_{3/2}$ region, similar peaks at 718.8, 714.7, 712.8, and 710.2 eV were found and attributed to Fe^{3+} (satellite), Fe^{2+} (satellite), Fe^{3+}, and Fe^{2+}, respectively. While the remaining

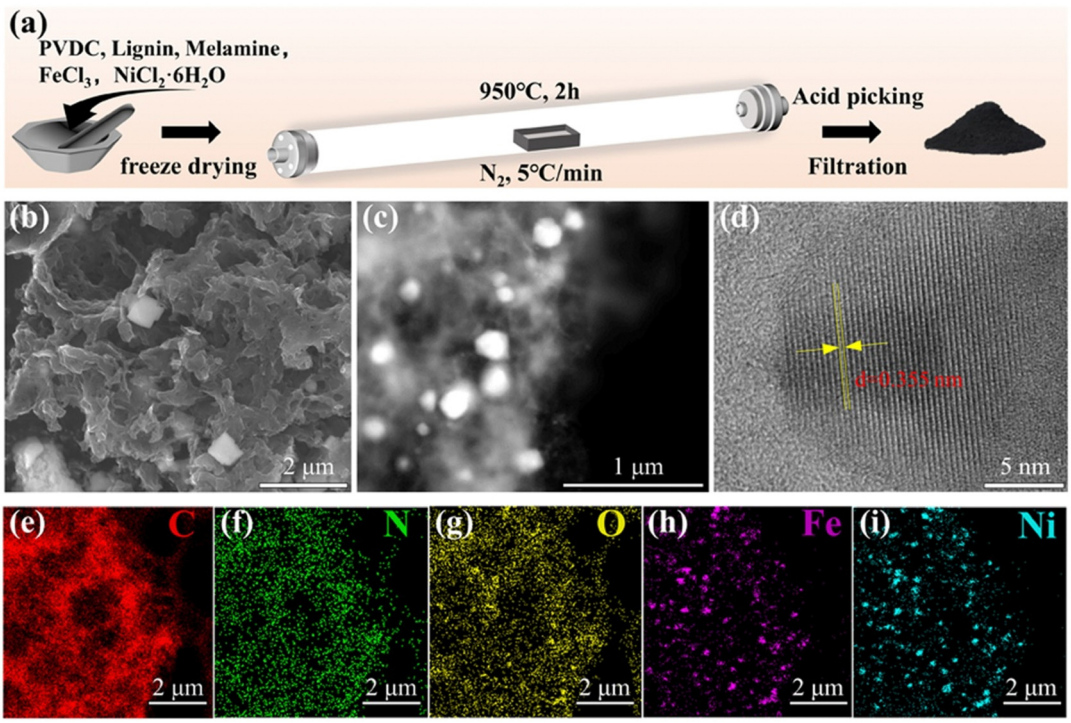

Fig. 1 (a) Schematic illustration of the synthesis procedure. (b) SEM, (c) HAADF-STEM, (d) HRTEM, and (e–i) elemental mapping images of FeNi/NC.

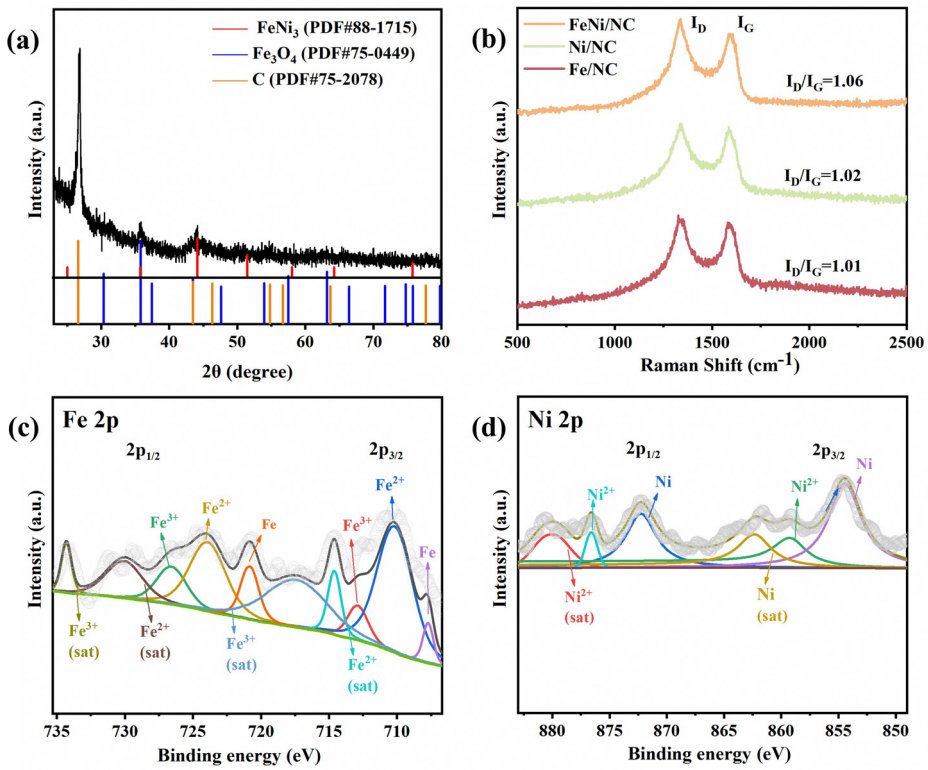

Fig. 2 (a) XRD pattern of FeNi/NC. (b) Raman spectra of FeNi/NC, Fe/NC, and Ni/NC. (c) Fe 2p and (d) Ni 2p XPS spectra of FeNi/NC.

peaks at 720.5 of Fe $2p_{1/2}$ and 707.7 eV of Fe $2p_{3/2}$ are assigned to Fe(0).[37] In the deconvolution analysis of Ni 2p XPS spectra (Fig. 2d), there are two groups of peaks of Ni^{2+} (876.6/859.2 eV) and Ni (872.2/854.4 eV) accompanied by two shake-up satellite peaks (879.9/862.3 eV) in the Ni $2p_{1/2}$ and Ni $2p_{3/2}$.[40]

The electrochemical performance of FeNi/NC, Fe/NC, and Ni/NC have been investigated by using a 0.1 M KNO_3 solution as the electrolyte, CO_2 as feeding gas were continuously bubbled into the H-shaped cell (Fig. S5, ESI†). Linear sweep voltammetry (LSV) curves for FeNi/NC, Fe/NC, and Ni/NC in Ar or CO_2 saturated electrolytes are shown in the Fig. 3a and Fig. S6 (ESI†). Their current densities from −0.2 to −1.4 V (*vs.* RHE) are significantly higher in CO_2-saturated electrolyte than in Ar-saturated electrolyte, and the current densities of FeNi/NC were higher than those of Fe/NC and Ni/NC, indicating FeNi/NC possess better electrocatalytic activity towards the synthesis of urea from CO_2 and NO_3^-. Meantime, the above three materials' electrochemical impedance spectroscopy (EIS) data (Fig. S7, ESI†) were also shown to analyze their kinetics properties. Both of them presented similar charger transfer resistance of ~20 Ω, while the slope of FeNi/NC in low frequency region was more vertical compared to the other two, which implies that it has the lowest Warburg impedance, fast ion diffusion and short diffusion distance.[41] And in the double-layer (C_{dl}) measurement (Fig. S8, ESI†), it can be observed that the C_{dl} value of FeNi/NC is about 1.3 times that of Fe/NC and 1.6 times that of Ni/NC, which implies that the former has a larger electrochemically active surface area (ECSA).[42]

To further quantitatively assess urea electrosynthesis activity, chronopotentiometry procedure with different applied potential from −0.8 to −1.1 V *vs.* RHE was carried out in CO_2 saturated 0.1 M KNO_3. The obtained liquid by-products, such NH_3 and NO_2^-, were estimated through chromogenic method, the corresponding calibration curves of them are shown in Fig. S9 and S10 (ESI†). While the generated urea was analyzed by the urease method according to the principle that 1 mol urea can be decomposed into 2 mol NH_3 (Fig. S11, ESI†).[43] Meanwhile, ^1H NMR was also employed to identify the produced urea and NH_3 after 1 h electrolysis at −0.9 V *vs.* RHE (Fig. S12 and S13, ESI†). Moreover, the gaseous products, such as H_2 and CO, were monitored by gas chromatography. As shown in Fig. 3b and c, the urea yield rate and corresponding FE on different potentials could be calculated through UV-vis spectra and corresponding calibration curve. It can be observed that as the applied potential increases, the urea yield rate and FE also increase, reaching a maximum yield of 496.5 μg h^{-1} $mg_{cat.}^{-1}$ and FE of 16.58% at −0.9 V (*vs.* RHE). FeNi/NC exhibited comparable or better urea production activity than previously reported catalysts (Table S1, ESI†). Furthermore, comparison of the variability of the crystalline compositions of the three catalysts mentioned above, it could be seen that FeNi/NC, Fe/NC, and Ni/NC each corresponded to $FeNi_3/Fe_3O_4$, Fe/Fe_3O_4, and Ni. Among them, the electrocatalytic activity, both in terms of urea yield and FE, was the highest in FeNi/NC, and it differed significantly from the other samples as follows the presence of $FeNi_3$ alloy nanoparticles, which implied that $FeNi_3$ part played

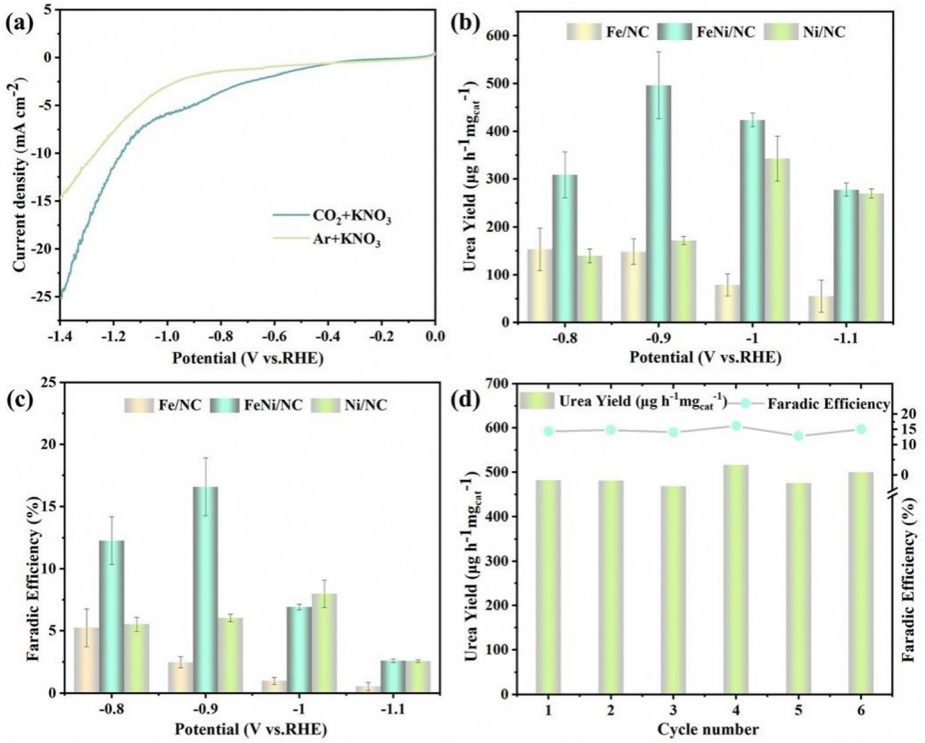

Fig. 3 (a) LSV curves of FeNi/NC measured in Ar and CO_2 saturated 0.1 M KNO_3 electrolytes. (b) The urea yield and (c) urea FE for FeNi/NC, Fe/NC, and Ni/NC on the different applied potentials. (d) The cyclic stability test of FeNi/NC for urea synthesis.

an indispensable role as an active part in the urea synthesis process.

However, these two values including yield and FE gradually decrease when the potential exceeds −0.9 V *vs.* RHE, mainly due to possible competitive hydrogen evolution reaction (HER), CO_2RR, and NO_3RR. To verify this speculation, all possible products during the electrocatalytic urea synthesis process were identified, including H_2, CO, NH_3, NO_2^-, and urea (Fig. S14, ESI†). It was found that the FE of the by-products increased significantly at higher negative potentials, leading to a poorer selectivity of urea. Subsequently, electrocatalytic stability tests of FeNi/NC, including cyclic experiments and chronoamperometry electrolysis, were carried out in CO_2-saturated 0.1 M KNO_3. The cyclic test was carried out for 6 cycles at −0.90 V *vs.* RHE with each cycle lasting 1 h of electrocatalysis and almost no decay in urea yield and FE (Fig. 3d), and the current density profile did not decay significantly after 30 h of continuity (Fig. S15, ESI†), showing the good reproducibility and durability of FeNi/NC materials. Also, after 30 h stability test, the XRD pattern and SEM image of the as-obtained FeNi/NC were demonstrated Fig. S16 and S17 (ESI†), respectively. It could be observed that the crystal structure and thinner carbon nanosheets morphology of FeNi/NC were well preserved, demonstrating its better robustness. In order to exclude the possible influence of environmental and chemical interferences on the experimental results, a series of control experiments were performed to further verify that the urea generated came from the simultaneous reduction of CO_2 and NO_3^- and not from pollutants: (i) open-circuit potential of FeNi/NC in CO_2-saturated 0.1 M KNO_3 for 1 h; (ii) chronoamperometry of FeNi/NC at −0.9 V (*vs.* RHE) in Ar-saturated 0.1 M KNO_3 for 1 h; (iii) chronoamperometry of FeNi/NC at −0.9 V (*vs.* RHE) in CO_2-saturated 0.1 M $KHCO_3$ for 1 h. In all three cases mentioned above, the absorbance of the two electrolytes (open circuit and blank electrolyte; with and without urease) was measured by UV-vis spectra, and no significant difference was found between them, which indicated that no urea was detected (Fig. S18 and S19, ESI†), suggesting that the urea generated *via* FeNi/NC catalysis was indeed from the coupling reaction of CO_2 and NO_3^-.

Moreover, electrochemical *in situ* Raman spectroscopy was employed to detect the evolution of bond structures of intermediate species generated during the electrocatalytic process of FeNi/NC (Fig. 4a and Fig. S20, ESI†). In a CO_2-saturated 0.1 M KNO_3 solution of Fig. 4b, compared to the noticeable characteristic peak of O–C–O antisymmetrical stretching at 1050 cm^{-1} originating from CO_3^{2-} in the open circuit potential,[44,45] peak intensity of other potential gradually decreases with higher applied potential from −0.8 V to −1.1 V (*vs.* RHE), indicating that growth in the consumption rate of CO_3^{2-}, which implies that for the urea synthesis provides sufficient key intermediates of *COOH and *CO.[43,46] Meanwhile, *in situ* Raman spectra also appeared a weak peak at 1000 cm^{-1} with prolonged electroreduction time (Fig. 4c and d),[47–49] which could be attributed to the N–C–N symmetric stretching model of the urea molecule and confirmed by the high concentration of the urea solution (Fig. S21, ESI†), indicating that a C–N coupling reaction between CO_2 and NO_3^- was indeed occurred.[50–56]

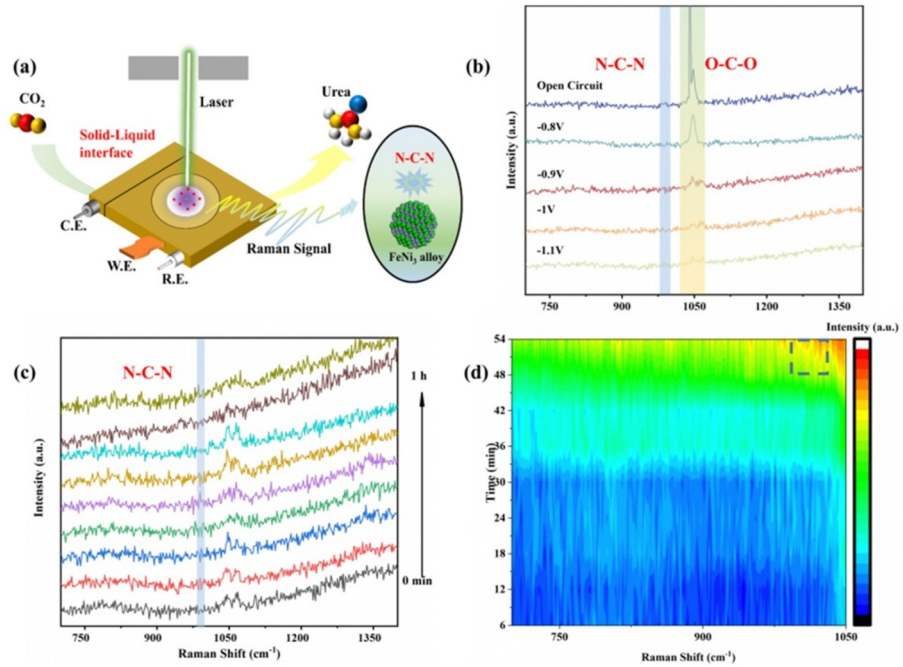

Fig. 4 (a) *In situ* Raman schematic diagram, (b) *in situ* Raman spectra at different potentials, (c) *in situ* Raman plots at different reaction time at −0.9 V *vs.* RHE, and (d) corresponding contour plots.

4. Conclusions

In summary, numerous $FeNi_3$ nanoparticles loaded on nitrogen-doped porous carbon were constructed through a simple carbonization strategy. Conductive carbon substrates with porous structures not only promote electrocatalytic kinetics, but also enhance full exposure of active sites. The obtained catalyst achieve the highest urea yield rate of 496.5 μg h^{-1} $mg_{cat.}^{-1}$ and FE of 16.58% in CO_2-saturated 0.1 M KNO_3 at −0.9 V *vs.* RHE. The *in situ* Raman spectroscopy and control experiments confirmed that the generated urea was originated from the C–N coupling reaction of CO_2 and NO_3^-.

Conflicts of interest

There are no conflicts to declare.

Acknowledgements

This work was financially supported by the National Natural Science Foundation of China (22075211 and 51971157), Shenzhen Science and Technology Program (JCYJ20210324123202008, JCYJ20210324122803009 and ZDSYS20210813095534001), Guangdong Basic and Applied Basic Research Foundation (2021A1515110880), and Tianjin Science Fund for Distinguished Young Scholars (19JCJQJC61800).

References

1 Y. Feng, H. Yang, Y. Zhang, X. Huang, L. Li, T. Cheng and Q. Shao, Te-Doped Pd Nanocrystal for Electrochemical Urea Production by Efficiently Coupling Carbon Dioxide Reduction with Nitrite Reduction, *Nano Lett.*, 2020, **20**, 8282–8289.

2 J. Li, G. Zhan, J. Yang, F. Quan, C. Mao, Y. Liu, B. Wang, F. Lei, L. Li, A. W. M. Chan, L. Xu, Y. Shi, Y. Du, W. Hao, P. K. Wong, J. Wang, S. X. Dou, L. Zhang and J. C. Yu, Efficient Ammonia Electrosynthesis from Nitrate on Strained Ruthenium Nanoclusters, *J. Am. Chem. Soc.*, 2020, **142**, 7036–7046.

3 Y. Huang, R. Yang, C. Wang, N. Meng, Y. Shi, Y. Yu and B. Zhang, Direct Electrosynthesis of Urea from Carbon Dioxide and Nitric Oxide, *ACS Energy Lett.*, 2021, **7**, 284–291.

4 L. Han, P. Ou, W. Liu, X. Wang, H.-T. Wang, R. Zhang, C.-W. Pao, X. Liu, W.-F. Pong, J. Song, Z. Zhuang, M. V. Mirkin, J. Luo and H. L. Xin, Design of Ru–Ni diatomic sites for efficient alkaline hydrogen oxidation, *Sci. Adv.*, 2022, **8**, eabm3779.

5 G.-F. Chen, Y. Yuan, H. Jiang, S.-Y. Ren, L.-X. Ding, L. Ma, T. Wu, J. Lu and H. Wang, Electrochemical reduction of nitrate to ammonia via direct eight-electron transfer using a copper–molecular solid catalyst, *Nat. Energy*, 2020, **5**, 605–613.

6 Y. Wang, Y. Yu, R. Jia, C. Zhang and B. Zhang, Electrochemical synthesis of nitric acid from air and ammonia through waste utilization, *Natl. Sci. Rev.*, 2019, **6**, 730–738.

7 S. Liu, M. Jin, J. Sun, Y. Qin, S. Gao, Y. Chen, S. Zhang, J. Luo and X. Liu, Coordination environment engineering to boost electrocatalytic CO_2 reduction performance by introducing boron into single-Fe-atomic catalyst, *Chem. Eng. J.*, 2022, **437**, 135294.

8 M. Yuan, J. Chen, Y. Bai, Z. Liu, J. Zhang, T. Zhao, Q. Wang, S. Li, H. He and G. Zhang, Unveiling Electrochemical Urea

Synthesis by Co-Activation of CO_2 and N_2 with Mott-Schottky Heterostructure Catalysts, *Angew. Chem., Int. Ed. Engl.*, 2021, **60**, 10910–10918.

9 C. Lv, C. Lee, L. Zhong, H. Liu, J. Liu, L. Yang, C. Yan, W. Yu, H. H. Hng, Z. Qi, L. Song, S. Li, K. P. Loh, Q. Yan and G. Yu, A Defect Engineered Electrocatalyst that Promotes High-Efficiency Urea Synthesis under Ambient Conditions, *ACS Nano*, 2022, **16**, 8213–8222.

10 S. Liu, L. Wang, H. Yang, S. Gao, Y. Liu, S. Zhang, Y. Chen, X. Liu and J. Luo, Nitrogen-Doped Carbon Polyhedrons Confined Fe–P Nanocrystals as High-Efficiency Bifunctional Catalysts for Aqueous Zn–CO_2 Batteries, *Small*, 2022, **18**, 2104965.

11 J. Lim, C. A. Fernández, S. W. Lee and M. C. Hatzell, Ammonia and Nitric Acid Demands for Fertilizer Use in 2050, *ACS Energy Lett.*, 2021, **6**, 3676–3685.

12 Ö. Yildirim, K. Nölker, K. Büker and R. Kleinschmidt, Chemical Conversion of Steel Mill Gases to Urea: An Analysis of Plant Capacity, *Chem. Ing. Tech.*, 2018, **90**, 1529–1535.

13 P. H. van Langevelde, I. Katsounaros and M. T. M. Koper, Electrocatalytic Nitrate Reduction for Sustainable Ammonia Production, *Joule*, 2021, **5**, 290–294.

14 N. Meng, X. Ma, C. Wang, Y. Wang, R. Yang, J. Shao, Y. Huang, Y. Xu, B. Zhang and Y. Yu, Oxide-Derived Core-Shell Cu@Zn Nanowires for Urea Electrosynthesis from Carbon Dioxide and Nitrate in Water, *ACS Nano*, 2022, **16**, 9095–9104.

15 N. Meng, Y. Huang, Y. Liu, Y. Yu and B. Zhang, Electrosynthesis of urea from nitrite and CO_2 over oxygen vacancy-rich ZnO porous nanosheets, *Cell Rep. Phys. Sci.*, 2021, **2**, 100697.

16 Y. Wang, X. Zheng and D. Wang, Design concept for electrocatalysts, *Nano Res.*, 2021, **15**, 1730–1752.

17 Y. Liu, X. Tu, X. Wei, D. Wang, X. Zhang, W. Chen, C. Chen and S. Wang, C-Bound or O-Bound Surface: Which One Boosts Electrocatalytic Urea Synthesis?, *Angew. Chem., Int. Ed. Engl.*, 2023, **62**, e202300387.

18 W. Song, L. Yue, X. Fan, Y. Luo, B. Ying, S. Sun, D. Zheng, Q. Liu, M. S. Hamdy and X. Sun, Recent progress and strategies on the design of catalysts for electrochemical ammonia synthesis from nitrate reduction, *Inorg. Chem. Front.*, 2023, **10**, 3489–3514.

19 L. Li, I. M. U. Hasan, Farwa, R. He, L. Peng, N. Xu, N. K. Niazi, J.-N. Zhang and J. Qiao, Copper as a single metal atom based photo-, electro-, and photoelectrochemical catalyst decorated on carbon nitride surface for efficient CO_2 reduction: a review, *Nano Res. Energy*, 2022, **1**, e9120015.

20 M. Yang, S. Liu, J. Sun, M. Jin, R. Fu, S. Zhang, H. Li, Z. Sun, J. Luo and X. Liu, Highly dispersed Bi clusters for efficient rechargeable Zn−CO_2 batteries, *Appl. Catal., B*, 2022, **307**, 121145.

21 J. Liang, Z. Li, L. Zhang, X. He, Y. Luo, D. Zheng, Y. Wang, T. Li, H. Yan, B. Ying, S. Sun, Q. Liu, M. S. Hamdy, B. Tang and X. Sun, Advances in ammonia electrosynthesis from ambient nitrate/nitrite reduction, *Chem*, 2023, **9**, 1768–1827.

22 Q. Liu, L. Xie, J. Liang, Y. Ren, Y. Wang, L. Zhang, L. Yue, T. Li, Y. Luo, N. Li, B. Tang, Y. Liu, S. Gao, A. A. Alshehri, I. Shakir, P. O. Agboola, Q. Kong, Q. Wang, D. Ma and X. Sun, Ambient Ammonia Synthesis via Electrochemical Reduction of Nitrate Enabled by $NiCo_2O_4$ Nanowire Array, *Small*, 2022, **18**, 2106961.

23 Y. Nakaya and S. Furukawa, Catalysis of Alloys: Classification, Principles, and Design for a Variety of Materials and Reactions, *Chem. Rev.*, 2023, **123**, 5859–5947.

24 X. Xu, L. Hu, Z. Li, L. Xie, S. Sun, L. Zhang, J. Li, Y. Luo, X. Yan, M. S. Hamdy, Q. Kong, X. Sun and Q. Liu, Oxygen vacancies in Co_3O_4 nanoarrays promote nitrate electroreduction for ammonia synthesis, *Sustainable Energy Fuels*, 2022, **6**, 4130–4136.

25 W. Zhang, M. Jiang, S. Yang, Y. Hu, B. Mu, Z. Tie and Z. Jin, In situ grown CuO_x nanowire forest on copper foam: A 3D hierarchical and freestanding electrocatalyst with enhanced carbonaceous product selectivity in CO_2 reduction, *Nano Res. Energy*, 2022, **1**, e9120033.

26 H. Wang, Y. Jiang, S. Li, F. Gou, X. Liu, Y. Jiang, W. Luo, W. Shen, R. He and M. Li, Realizing efficient C–N coupling via electrochemical co-reduction of CO_2 and NO_3^- on AuPd nanoalloy to form urea: Key C–N coupling intermediates, *Appl. Catal., B*, 2022, **318**, 121819.

27 C. Chen, X. Zhu, X. Wen, Y. Zhou, L. Zhou, H. Li, L. Tao, Q. Li, S. Du, T. Liu, D. Yan, C. Xie, Y. Zou, Y. Wang, R. Chen, J. Huo, Y. Li, J. Cheng, H. Su, X. Zhao, W. Cheng, Q. Liu, H. Lin, J. Luo, J. Chen, M. Dong, K. Cheng, C. Li and S. Wang, Coupling N_2 and CO_2 in H_2O to synthesize urea under ambient conditions, *Nat. Chem.*, 2020, **12**, 717–724.

28 Z. Li, J. Liang, Q. Liu, L. Xie, L. Zhang, Y. Ren, L. Yue, N. Li, B. Tang, A. A. Alshehri, M. S. Hamdy, Y. Luo, Q. Kong and X. Sun, High-efficiency ammonia electrosynthesis via selective reduction of nitrate on $ZnCo_2O_4$ nanosheet array, *Mater. Today Phys.*, 2022, **23**, 100619.

29 K. Chen, M. Cao, G. Ni, S. Chen, H. Liao, L. Zhu, H. Li, J. Fu, J. Hu, E. Cortés and M. Liu, Nickel polyphthalocyanine with electronic localization at the nickel site for enhanced CO_2 reduction reaction, *Appl. Catal., B*, 2022, **306**, 121093.

30 Q. Lu, C. Chen, Q. Di, W. Liu, X. Sun, Y. Tuo, Y. Zhou, Y. Pan, X. Feng, L. Li, D. Chen and J. Zhang, Dual Role of Pyridinic-N Doping in Carbon-Coated Ni Nanoparticles for Highly Efficient Electrochemical CO_2 Reduction to CO over a Wide Potential Range, *ACS Catal.*, 2022, **12**, 1364–1374.

31 H. Zhang, C. Wang, H. Luo, J. Chen, M. Kuang and J. Yang, Iron Nanoparticles Protected by Chainmail-structured Graphene for Durable Electrocatalytic Nitrate Reduction to Nitrogen, *Angew. Chem., Int. Ed. Engl.*, 2023, **62**, e202217071.

32 J. Wang, Y. Wang, C. Cai, Y. Liu, D. Wu, M. Wang, M. Li, X. Wei, M. Shao and M. Gu, Cu-Doped Iron Oxide for the Efficient Electrocatalytic Nitrate Reduction Reaction, *Nano Lett.*, 2023, **23**, 1897–1903.

33 S. Zhang, M. Li, J. Li, Q. Song and X. Liu, High-ammonia selective metal-organic framework-derived Co-doped Fe/Fe_2O_3 catalysts for electrochemical nitrate reduction, *Proc. Natl. Acad. Sci. U. S. A.*, 2022, **119**, e2115504119.

34 G. Zhang, L. Wang, Y. Hao, X. Jin, Y. Xu, Y. Kuang, L. Dai and X. Sun, Unconventional Carbon: Alkaline Dehalogenation of Polymers Yields N-Doped Carbon Electrode for High-Performance Capacitive Energy Storage, *Adv. Funct. Mater.*, 2016, **26**, 3340–3348.

35 Y. Ge and Z. Li, Application of Lignin and Its Derivatives in Adsorption of Heavy Metal Ions in Water: A Review, *ACS Sustainable Chem. Eng.*, 2018, **6**, 7181–7192.

36 N. Supanchaiyamat, K. Jetsrisuparb, J. T. N. Knijnenburg, D. C. W. Tsang and A. J. Hunt, Lignin materials for adsorption: Current trend, perspectives and opportunities, *Bioresour. Technol.*, 2019, **272**, 570–581.

37 J. Geng, S. Ji, M. Jin, C. Zhang, M. Xu, G. Wang, C. Liang and H. Zhang, Ambient Electrosynthesis of Urea with Nitrate and Carbon Dioxide over Iron-Based Dual-Sites, *Angew. Chem., Int. Ed. Engl.*, 2023, **62**, e202210958.

38 W. Ma, X. He, W. Wang, S. Xie, Q. Zhang and Y. Wang, Electrocatalytic reduction of CO_2 and CO to multi-carbon compounds over Cu-based catalysts, *Chem. Soc. Rev.*, 2021, **50**, 12897–12914.

39 J. Ding, Q. Sun, L. Zhong, X. Wang, L. Chai, Q. Li, T.-T. Li, Y. Hu, J. Qian and S. Huang, Thermal conversion of hollow nickel-organic framework into bimetallic $FeNi_3$ alloy embedded in carbon materials as efficient oer electrocatalyst, *Electrochim. Acta*, 2020, **354**, 136716.

40 Y. Wang, G. Qian, Q. Xu, H. Zhang, F. Shen, L. Luo and S. Yin, Industrially promising IrNi–$FeNi_3$ hybrid nanosheets for overall water splitting catalysis at large current density, *Appl. Catal., B*, 2021, **286**, 119881.

41 X. Wang, W. Zhang, Q. Yu, X. Liu, Q. Liang, X. Meng, X. Wang and L. Wang, Fe-doped CoNiP@N-doped carbon nanosheet arrays for hydrazine oxidation assisting energy-saving seawater splitting, *Chem. Eng. J.*, 2022, **446**, 136987.

42 D. Qi, F. Lv, T. Wei, M. Jin, G. Meng, S. Zhang, Q. Liu, W. Liu, D. Ma, M. S. Hamdy, J. Luo and X. Liu, High-efficiency electrocatalytic NO reduction to NH_3 by nanoporous VN, *Nano Res. Energy*, 2022, **1**, e9120022.

43 X. Zhang, X. Zhu, S. Bo, C. Chen, M. Qiu, X. Wei, N. He, C. Xie, W. Chen, J. Zheng, P. Chen, S. P. Jiang, Y. Li, Q. Liu and S. Wang, Identifying and tailoring C–N coupling site for efficient urea synthesis over diatomic Fe–Ni catalyst, *Nat. Commun.*, 2022, **13**, 5337.

44 P. Li, J. Bi, J. Liu, Y. Wang, X. Kang, X. Sun, J. Zhang, Z. Liu, Q. Zhu and B. Han, p–d Orbital Hybridization Induced by p-Block Metal-Doped Cu Promotes the Formation of C^{2+} Products in Ampere-Level CO_2 Electroreduction, *J. Am. Chem. Soc.*, 2023, **145**, 4675–4682.

45 W. Shan, R. Liu, H. Zhao, Z. He, Y. Lai, S. Li, G. He and J. Liu, In Situ Surface-Enhanced Raman Spectroscopic Evidence on the Origin of Selectivity in CO_2 Electrocatalytic Reduction, *ACS Nano*, 2020, **14**, 11363–11372.

46 V. Fawcett and D. A. Long, Raman spectroscopic studies of urea/n-paraffin clathrates, *J. Raman Spectrosc.*, 1975, **3**, 263–275.

47 P. Shen, X. Li, Y. Luo, N. Zhang, X. Zhao and K. Chu, Ultra-efficient N_2 electroreduction achieved over a rhodium single-atom catalyst (Rh_1/MnO_2) in water-in-salt electrolyte, *Appl. Catal., B*, 2022, **316**, 121651.

48 J. Liang, Q. Liu, A. A. Alshehri and X. Sun, Recent advances in nanostructured heterogeneous catalysts for N-cycle electrocatalysis, *Nano Res. Energy*, 2022, **1**, e9120010.

49 Z. Wang, D. Richards and N. Singh, Recent discoveries in the reaction mechanism of heterogeneous electrocatalytic nitrate reduction, *Catal. Sci. Technol.*, 2021, **11**, 705–725.

50 J. Shao, N. Meng, Y. Wang, B. Zhang, K. Yang, C. Liu, Y. Yu and B. Zhang, Scalable Electrosynthesis of Formamide through C−N Coupling at the Industrially Relevant Current Density of 120 $mA\,cm^{-2}$, *Angew. Chem., Int. Ed.*, 2022, **61**, e202213009.

51 Y. Huang, Y. Wang, Y. Wu, Y. Yu and B. Zhang, Electrocatalytic construction of the C–N bond from the derivates of CO_2 and N_2, *Sci. China: Chem.*, 2022, **65**, 204–206.

52 Q. Zhang, K. Lian, Q. Liu, G. Qi, S. Zhang, J. Luo and X. Li, High entropy alloy nanoparticles as efficient catalysts for alkaline overall seawater splitting and Zn–air batteries, *J. Colloid Interface Sci.*, 2023, **646**, 844–854.

53 S. Zhang, Q. Liu, X. Tang, Z. Zhou, T. Fan, Y. You, Q. Zhang, S. Zhang, J. Luo and X. Li, Electrocatalytic reduction of NO to NH_3 in ionic liquids by P-doped TiO_2 nanotubes, *Front. Chem. Sci. Eng.*, 2023, **17**, 726–734.

54 M. Tang, Q. Tong, Y. Li, R. Jiang, L. Shi, F. Shen, Y. Wei, Z. Liu, S. Liu, J. Zhang and G. Jiang, Effective and selective electrocatalytic nitrate reduction to ammonia on urchin-like and defect-enriched titanium oxide microparticles, *Chin. Chem. Lett.*, 2023, 108410.

55 W. Zhang, X. Qin, T. Wei, Q. Liu, J. Luo and X. Liu, Single atomic cerium sites anchored on nitrogen-doped hollow carbon spheres for highly selective electroreduction of nitric oxide to ammonia, *J. Colloid Interface Sci.*, 2023, **638**, 650–657.

56 T. Feng, F. Li, X. Hu and Y. Wang, Selective electroreduction of nitrate to ammonia via $NbWO_6$ perovskite nanosheets with oxygen vacancy, Chinese, *Chem. Lett.*, 2023, **34**, 107862.

